Nanoscale

ROYAL SOCIETY OF CHEMISTRY

PAPER

Cite this: *Nanoscale*, 2024, **16**, 15758

Nano–microcrystals revealed on Tang dynasty gilded bronze using advanced TEM–SEM and synchrotron methods†

Ioannis Liritzis, *[a,b] Sophie Cazottes,[c] Thierry Douillard, [c] Muriel Véron,[d] Josep Roqué-Rosell,[e] Carlo Marini,[e] Partha Pratim Das, [f] Alejandro Gomez-Perez,[f] Athanassios S. Galanis,[f] Stavros Nicolopoulos,[f] Panagiota Manti, [g] Junchang Yang[h] and Xiangyu Zhang[i]

Over the years, numerous gold and silver artifacts have been excavated from the tombs of the Tang dynasty, which give evidence of the sophisticated metalworking techniques at that time. Few of the artifacts were thoroughly studied and their manufacturing processes were barely known. The present investigation concerns a metal headgear from a newly excavated tomb of a female in Xi'an of the Tang dynasty (618–907 A.D.), using advanced techniques in a complementary way, especially performing a detailed analysis of the corrosion products and alloying processes. The combined state-of-the-art methods and instrumentation used for the corrosion study included spectroscopy, diffraction, electron microscopy, synchrotron and their versions for specific measurements and sample preparation. The investigated headgear metal consists of a copper-based core, which is gilded by a thin gold layer, consisting of an Au–Hg alloy with a thin layer of about 400 nm. The technique used for shaping and hammered embellishments led to the creation of nanosized grains on the side that would eventually be the interior of the headgear. It was gilded using the mercury-amalgamation process, and the liquid diffusion caused the development of intermetallic compounds. This is the first recorded instance of these nano-scale and eutectic phases being observed on objects from an archaeological context. The crystallographic analysis offered valuable insights into the formation of needle-like malachite crystals growing on a layer of cuprite found on the surface of the corroded piece. The results highlight that the artisans utilized advanced methods in the creation of funerary items during the Tang dynasty.

Received 10th May 2024,
Accepted 24th July 2024

DOI: 10.1039/d4nr02030h

rsc.li/nanoscale

1. Introduction

Gilding was employed, as the last step in Tang dynasty metallurgy, to create a glossy, gold layer on the completed object. Information about the material properties and manufacturing processes used to create such golden and silver goods has previously been published.[1–10] A range of metalworking methods were employed throughout the Tang dynasty, but more consistent research is needed to identify advancements.

Mercury gilding used less gold than other procedures to produce a strong gold coating, and it was a popular method of gold plating in ancient China[11] and in other parts of the world.[12–14] Gold was an expensive metal of status, leading to the development of techniques of making cheaper objects appearing like gold,[15] such as foil gilding, using gold inlays, and fire gilding.[1,2,16] Fire-gilding first appeared in China in the 4th century B.C.[17,18] and it became one of the most popular metal surface decorating techniques in ancient China.[4,19] The method involves the use of mercury with gold;

[a]*Laboratory of Yellow River Cultural Heritage, Key Research Institute of Yellow River Civilization and Sustainable Development & Collaborative Innovation Center on Yellow River Civilization, Henan University, Kaifeng 475001Minglun Road 85, China. E-mail: liritzis@henu.edu.cn*
[b]*Alma Mater Europaea (AMEU) – ECM, Slovenska Ulica 17, 2000 Maribor, Slovenia*
[c]*Univ Lyon, INSA Lyon, CNRS, MATEIS, UMR 5510, 69621, 20 Avenue Albert Einstein, Villeurbanne Cedex 69621, France*
[d]*SIMAP Laboratory, CNRS-Grenoble INP, BP 46 101 rue de la Physique, 38402 Saint Martin d'Hères, France*
[e]*ALBA Synchrotron Light Source & Univ. of Barcelona, Spain*
[f]*NanoMEGAS SPRL, Rue Émile Claus 49 bte 9, 1050 Brussels, Belgium*
[g]*Department of Environment, Ionian University, Zakynthos, Greece*
[h]*Research Centre of Material Science and Archaeology, Institute of Culture and Heritage, Northwestern Polytechnical University, Xi'an, China. E-mail: yangjunchang@nwpu.edu.cn*
[i]*Xi'an Institute of Conservation and Archaeology, 710068 Xi'an, China*
† Electronic supplementary information (ESI) available. See DOI: https://doi.org/10.1039/d4nr02030h

mercury chemically dissolves gold to create an amalgam.[20,21] The Au–Hg amalgam enables the application of a thin layer of gold uniformly on the surface of decorated items, which speeds up the gilding process and significantly reduces the amount of gold needed.[22,23] During amalgam gilding, the base metal is covered with the Au–Hg amalgam; next, mercury is evaporated by heating, leaving a gold layer on the base metal's surface.[24] As a result of mercury evaporating during the heating process, a porous structure is formed in the gold film. In addition, because of the Au–Hg system's solid–solution properties, mercury cannot be eliminated; instead, a small and fluctuating quantity of mercury remains and combines with gold to produce an alloy, the whole process realised after expert control of heating temperature.[11,25] As a result, the distinctive technical features of mercury gilding are its granular structure and residual mercury, which can be used to distinguish it from other gilding and plating methods.[10]

Several plated objects have been uncovered over time from Tang dynasty tombs, offering evidence for the use of advanced decorating methods during the period. Relatively few ancient objects have been examined scientifically, and little is known about the making and decoration methods used.[26] Many studies on ancient Chinese gilding technology focus on textual analysis of the process and determination of gilded goods, based on the literary research rather than the scientific analysis of excavated objects.[9,11] Every investigation on gilded bronze in China provides evidence to confirm current understandings and offers new evidence on the technologies employed for shaping and decoration methods.[27–31]

This work focuses on the metal headgear excavated from the tomb of a female and uses advanced techniques in a complementary way. Metallographic analysis aims to understand the microstructure of the metal and offer understanding about the shaping and gilding method, including evidence of hammering and annealing, the nature and thickness of the gold coating, and the presence of mercury. The methodology includes a range of complementary techniques used also in cultural heritage research.[32,33] The chemical composition, the morphology and the mineralogy of the corrosion products and gilding were investigated using OM, SEM–BSE, SEM–FEG, EBSD, TEM–EDS, TEM–ASTAR, 3D-ED and synchrontron XRF and XANES techniques. It is the first time that these combined methods are employed to understand the evidence of metal shaping, gilding and archaeological copper corrosion at a nanoscale.

2. Experimental

2.1. Archaeological materials

The recently excavated burial site Xingfulindai in Xi'an (Shaanxi province) unearthed amongst others a Tang dynasty tomb of a female (618–907 A.D.) with a fragmentary gilded copper alloy headgear. Artifacts from this site are analysed for the first time in our present work. The use of metal headdresses (gold, silver, or bronze) by high-ranking females complied with the sumptuary rules in the Tang dynasty, and it is likely that the gilded headgear was deposited in the funerary context in an attempt to imitate a real gold headgear. This fragmentary gilded headgear offers a great opportunity to investigate the gilding technology in the golden age of Tang dynasty China. With permission by our co-author excavator Mr Xiangyu Zhang, three fragments were selected to be analysed (Fig. 1): two pieces (Fig. 1a and b) and then an additional smaller one (Fig. 1c). Based on visual observation it appears that gilding was applied on the outer surface, evidently in the sample C fragment. Fragments A and B are expected to have evidence of gilding on the outer surface, but are covered by copper-based corrosion. The synchrotron experiment was done on two fragments: A and C. Fragment B was used for OM, SEM, EBSD, TEM–ASTAR, 3D-ED and EDS.

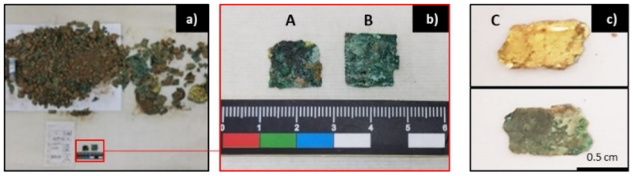

Fig. 1 Description of analysed fragments. (a) Copper-based headgear ornamental fragments as was found which contains pieces of plated gold and copper alloys mixed with sediments. (b) Largest analysed fragments with graduated scale (both sides are corroded. A-referenced fragment (left) was used for synchrotron measurements (one side were measured) whereas B-referenced fragment was used for experiments managed using scanning or transmission electron microscopy (the thickness of sample B is *ca.* 350 μm and a cross-section was made so that the two corroded sides could be analysed). (c) 3rd fragment, subjected to synchrotron measurements (the smallest, with one side gold plated and the other side corroded).

2.2. Sample preparation

The surfaces of fragments A and B were examined 'as received' by optical microscopy, scanning electron microscopy, and synchrotron XRF and XANES. The preparation of fragment B for analysis by scanning electron microscopy was done using ionic polishing with a broad argon beam. Argon broad ion beam (BIB) polishing is a good way to prepare high quality surfaces suitable for high resolution SEM–FEG imaging and EBSD analysis. BIB instruments are mostly bench-top systems designed to produce cross-section SEM–FEG specimens with large areas. The model we used is an Ilion II (model 697, Gatan Inc., Pleasanton, US). For this apparatus, ion polishing is done by two variable-angle Penning ion guns (PIGs). These PIGs, supplied with argon gas, can produce variable beam energies from 8 keV down to 100 eV. They provide high current density (up to 10 mA cm^{-2}) together with a spot size of about 1 mm whatever the energy. Thus, they allow high milling rates to be attained. For cross-section preparation, the two argon ion beams glance off a metal shield, creating a planar milling field. As the ion beam is partially blocked by this sputter-resistant blade, the resultant milling area propagates in a flat and horizontal plane above the blade edge.

To achieve cross-sectioning, the specimen is glued to the masking blade with silver glue so that a small part (50–100 μm) of the sample is left visible above the edge of the mask and the broad argon ion beam is aligned perpendicular to the edge. During standard operation, the specimen mount rotates continuously through 360°. Each gun fires once every rotation when the blade faces the gun. The gun fires between −30° and +30° with respect to the blade face. This minimizes curtaining caused by differential sputter rates of sample regions. This sector milling method modulates the dual ion guns to also minimize sample heating. In this study, BIB (broad ion beam) was used in cross-section polishing mode to make part of one side of fragment B suitable for SEM/FEG–EBSD–EDS analyses (the surface more than 1 mm wide over the entire section). This operation was performed with decreasing energies from 5 keV to 0.5 keV with the rate of 7 hours at 5 keV, 2 hours at 2 keV and 1 hour at 500 V. The cross-section observed is located on the edge of fragment B, in a corner (Fig. 2). This cross-section opens out on both corroded sides of the fragment and extends for just over 2 mm.

The sample preparation capabilities of FIB/SEM (FIB stands for focus ion beam) upgraded with *in situ* nano-robotic manipulators (NRMs) and a gas injection system (GIS) have been widely reviewed over recent years.[34] These well-equipped instruments offer considerable flexibility for preparing thin foils for TEM experiments. We have taken advantage of this lift-out procedure, at several specific sites, which are identified on the BIB cross-section of fragment B (see further). These TEM sample preparations were performed using a gallium FIB/SEM–FEG dual beam (FEI Strata DB 235) at IMEN laboratory in Lille, France. The typical dimension of the TEM lamellas extracted from fragment B is 20 μm by several microns.

2.3. Methodology and instrumentation

The following instruments and methods were employed for the detailed analysis and in-depth investigation of the gilded bronze, as well as for the chemical composition, microstructure, and phase identification.

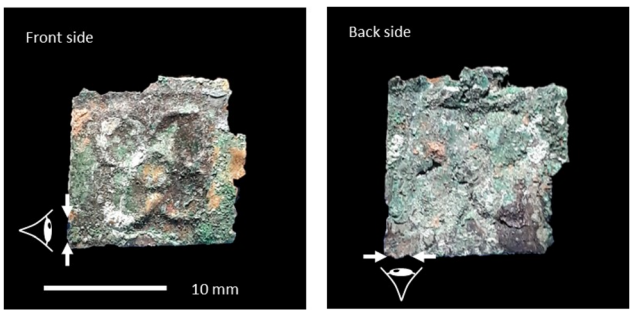

Fig. 2 Fragment B of Fig. 1b (B) used for cross-section preparation by BIB. The cross-section is located at a corner and on one edge of the fragment, between the white arrows. On both sides of the fragment, an eye icon indicates where the SEM–FEG analyses were performed. On these photographs, a decoration is visible in the form of a 4-petal flower (source: MATEIS/INSA).

Optical microscopy (OM). Light microscopy observations were conducted on the as-discovered material, using a Zeiss Axiophot microscope and an Axiocam digital camera (Jena, Germany), in bright or dark-field modes. OM was conducted at INSA Institute, Lyon, France.

Scanning electron microscopy (SEM–FEG) coupled with EBSD and EDS. The as-received surfaces and BIB cross-section of fragment B were examined using a SEM (Zeiss Gemini I column, Oberkochen, Germany). SEM–BSE images of the as-received surfaces were captured using a partial vacuum of 15 Pa of gaseous N_2 at 20 kV. For the cross-section, low energy SEM–BSE images were recorded at 1.5 kV and offer strong crystallographic contrast. EBSD crystallographic orientation maps were acquired on the cross-section using an Oxford Instruments EBSD symmetry camera (Abingdon-on-Thames, UK) with an accelerating voltage of 12 or 15 keV. The EBSD data were post-processed using Oxford Channel 5 software, with the crystallographic phases detailed in the ESI S2.† Note that EBSD cannot be used as a tool to identify the structures present in a material. Instead, data treatment allows one to find, among the number of structures assumed to be present, the best match between the theoretical and experimental patterns. If the declared structures are close to the ones present in the material, or if concrete orientation patterns match, solutions can be found and will be given as structures present in the sample.[35]

Energy dispersive X-ray spectrometry (EDS) chemical maps were prepared using a 50 mm^2 silicon drift detector (Oxford Instruments, High Wycombe, UK) in the SEM–FEG at acceleration voltages ranging from 10 keV to 30 keV. SEM–EDS analyses provide the local chemical composition (of a volume of the order of 1 μm^3) provided that the elements present are in sufficient concentration (typically from a few fractions of a percent) and that they are sufficiently heavy (detection of elements from Z = 5 boron upwards). This spectroscopy involves using the incident electron beam to excite the electrons in the material to be analysed so that when they return to their stable state, they emit secondary X-rays characteristic of the elements present. EBSD and EDS were conducted at the INSA Laboratory.

Transmission electron microscopy (TEM) EDS and ASTAR. A JEOL 2100F TEM operating at 200 kV (and equipped with a 60 mm^2 Jeol Centuiro EDS detector) was used at SIMAP Laboratory, and an FEI Tecnai G20 TEM at Nanomegas Laboratory, both equipped with an ASTAR device. A scanning transmission electron microscopy (STEM) option for TEM is located at the SIMAP Laboratory. ASTAR allows orientation and phase mapping at a nanometer scale (automated crystal orientation mapping, ACOM) with a spatial resolution of 1–5 nm where electron diffraction patterns combined with beam precession are matched with predefined phases by a template matching procedure resulting in phase and orientation maps.[36–38] The STEM–EDS and ASTAR procedure was performed at SIMAP Laboratory, Crenoble.

TEM 3-dimensional electron diffraction (3D-ED). The novel TEM based technique called 3D-ED (three-dimensional electron diffraction) has been employed to analyse nanometer size crystal.[39] The technique consists of collecting and processing 3D-ED data from single nanocrystals and is based on sampling the reciprocal space for the examined crystal in small steps (usually 1° tilt or less) or with continuous rotation of the crystal without any prior information on the structure and orientation of such crystal. The only essential requirement is that the data should be collected from the same crystal, in such a way that large numbers of reflections are typically recorded through a tilt around an arbitrary axis. During the data acquisition a small beam precession is used to reduce dynamical effects and better integration of the reflections In general, a tilting range of the specimen from −60° to +60° along the goniometer axis with a tilting step of 1° is an optimal compromise; this way, a total tilt wedge of 120° can be recorded, providing 121 diffraction patterns, which are usually enough for unit cell, symmetry, and crystal structure determination.[40] 3D-ED TEM measurements were conducted at the NanoMEGAS Laboratory.

XRF mapping and XANES. XRF mapping and XANES analysis determined the speciation of the core metal at CLAESS, the dedicated hard X-ray absorption beamline at ALBA synchrotron source Barcelona, Spain.[41,42] CLAESS beamline provides the required energy range (2.4–63.2 keV) with a small enough beam to perform XANES on the wide range of corrosion products present on the corroded surface.[41] The XRF mapping displaying elemental chemical analysis was obtained by rastering a selected 3 × 3 mm surface of the front of the fragment with a 50 μm at 12.5 keV X-ray beam in fluorescence geometry. To further understand the distribution and chemical variations of copper species on the surface of the fragment, point Cu K-edge XANES, by scanning 300 eV above its absorption edge, was acquired to gain understanding of their formation.

Summary of methodology and objectives. The investigation tries to understand the following issues:

- bulk surface examination of heterogeneous oxide corrosion products of present burial context present by OM, SEM–FEG, and SEM–EDS,
- overall bronze chemical changes, associated with the corrosion layer development, have been determined by means of synchrotron XRF and XANES,
- the characterization of the cross-section of the fragment to analyse in detail the profile of the thin metal sheet to reveal the technique of gilding and corrosion products by SEM–EDS, EBSD, OM, SEM–FEG, ASTAR, and 3D-ED,
- identification, determination, and characterization of the gold layer by TEM–EDS, ASTAR, 3D-ED, and ASTAR,
- the investigation of the core metal was conducted to reveal details of the manufacturing process. Analysis at a nanoscale would offer evidence of the eutectic phases formed during gilding using EBSD, OM, SEM–BSE, and TEM–high-angle annular dark-field imaging (HAADF) made by STEM, TEM–EDS, and ASTAR phase maps.

3. Results

3.1. Characterisation of surface corrosion products by optical/electron microscopy and EDS spectroscopy on the as-found fragment

The surface of the sample is heterogeneous; several types of oxides are visible under optical microscopy. On the surface of the core copper metal headgear artifact, the corrosion products display pale green, darker green, dark blue and brown colours (Fig. 3 and referred to Fig. 4 and 5). These result from the oxidation and corrosion of the metal core in the burial. The crystals constituting the corrosion layer nucleated and grew on the surface, mainly in the form of copper oxides, copper carbonates, and copper chlorides at the expense of core metal and due to copper dissolution.[43] Surface corrosion products appear globular under optical microscopy, but SEM imaging reveals that they are made up of clusters of acicular crystals (Fig. 4). The morphologies of these needle-like crystals[44] are shown in Fig. 5.

Apparent non-corroded areas were observed on the surface, thanks to a BSE *Z*-contrast. These areas appear brighter than the rest of the surface (Fig. 6). Local SEM–EDS measurements indicated that it contains gold and some mercury. Some copper was also detected, with a small amount of oxygen. The precise amount of Hg in this layer could not be measured using SEM–EDS, but the results show evidence that Au–Hg amalgam gilding was employed.

3.2. Characterisation of surface corrosion products by synchrotron radiation-based XRF and XANES on an as-found fragment

Elemental distribution maps were obtained by SR–XRF over fragment A (Fig. 7). The AuL_3 signal appears weak since it is thought to be hindered by the presence of copper corrosion layers. An increase of Cl content is observed at the border of

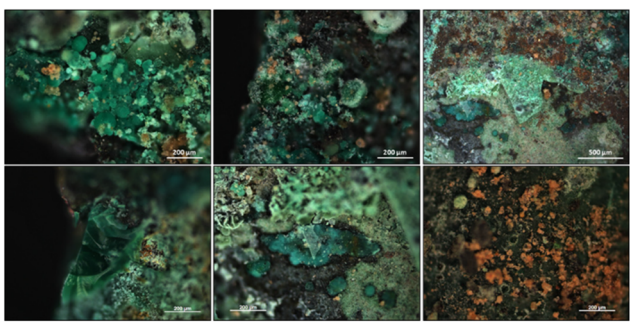

Fig. 3 Dark field optical micrographs taken on the surface of the B fragment. Surface corrosion products appear globular under optical microscopy, but SEM imaging reveals that they are made up of clusters of acicular crystals (Fig. 4). The morphologies of these needle-like crystals[44] vary from one place to another (Fig. 5), but their composition analysed with EDS shows that they are composed mainly of copper and oxygen. The elements also present, but in fluctuating quantities from one cluster to another, are: C, Mg, Al, Si, P, S, Ca and Fe (source: MATEIS/INSA).

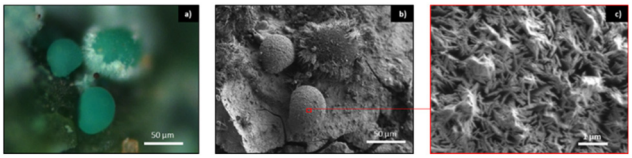

Fig. 4 Analysis of a surface corrosion product. (a) Dark field optical micrograph of an area with corrosion products on the surface of the B fragment and (b) the same field imaged in SEM (secondary electron imaging). (c) Close-up SEM view showing the morphology of acicular crystals. Although on the optical image certain corrosion products appear to be massively round, SEM imaging shows that in reality they are clusters of acicular crystals. An EDS analysis of the field shown in (c) reveals the presence of Cu and O. To a lesser extent, the elements C, Mg, Al, Si, P, S and Ca are also detected (source: MATEIS/INSA).

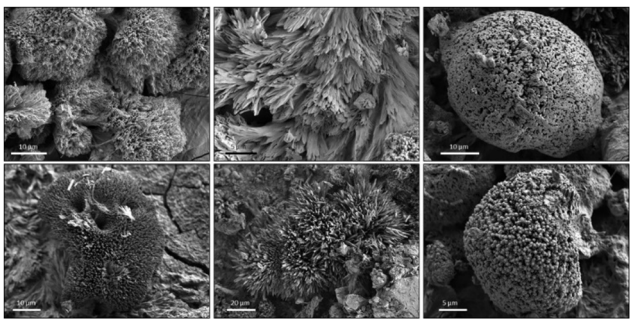

Fig. 5 SEM imaging of different acicular morphology found in corrosion products on the surface of the B fragment. EDS analyses carried out on these crystal clusters always show copper and oxygen to be the predominant elements. The elements C, Mg, Al, Si, P, S, Ca and Fe are almost always detected, but in fluctuating proportions (source: MATEIS/INSA).

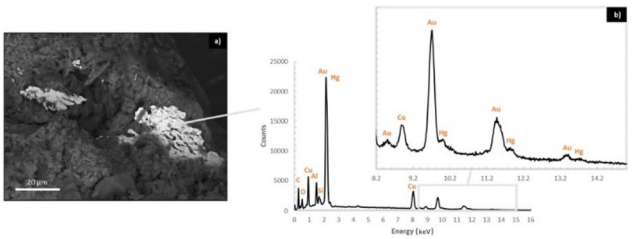

Fig. 6 Detection of gold flakes left uncovered by corrosion products. (a) SEM imaging (backscattered electron) in VP mode (15 Pa) showing bright (*i.e.* high *Z* number) flakes. (b) SEM–EDS spectrum corresponding to a spot on a bright flake. This phase is a gold layer containing mercury (Hg) (source: MATEIS/INSA).

the sample. The absence of Sn in the measurements is notable, suggesting that the object is not alloyed with tin. To gain a deeper understanding of the X-ray fluorescence (XRF) elemental distribution observed in the corroded fragment A, simulations of the X-ray penetration depth at 12.5 keV were conducted.[45] Various compositions were employed, including pure Cu, pure Au metals, and an Au_5Hg alloy. Assuming a scenario where the sample consists solely of metallic Cu, the X-ray beam would penetrate approximately 20 μm. In essence,

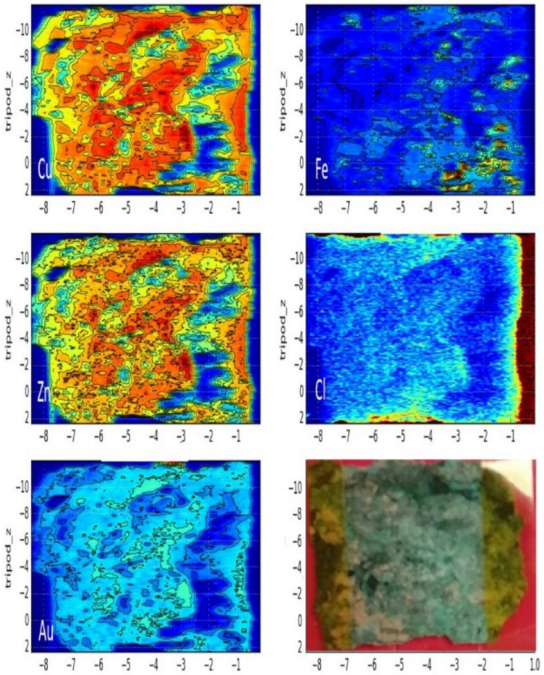

Fig. 7 Whole sample A (Fig. 1a) XRF mapping using a 50 micron @12 500 eV beam displaying the fluorescence signal distribution of Cu Kα, Zn Kα, Au L3, Fe Kα and Cl Kα. An increase of Cl content is observed at the border of the sample associated with Cu. No trace of Sn is observed. Hg mapping was not possible. Warmer colors mean higher fluorescence signal from the selected element (source: Josep Roqué Rosell).

this implies that our measurements are confined to the surface of the 350 μm thick sample, and any underlying pure metallic Au would remain unprobed. However, if the Au layer is exposed, the X-ray penetration depth diminishes to about 10 μm. In the case of an alloy with a composition like that of Au_5Hg, the penetration depth becomes even shallower, around 1 μm. Nevertheless, despite reaching the Au-rich layer with X-rays, the presence of any Cu or corrosion materials would impede the fluorescence signal[45] emitted from Au or Hg. This underscores the significance of the sample's composition and the potential influence of Cu residual materials on accurate Au and Hg fluorescence signal detection.

The signal distribution of CuKα on the heavily corroded fragment A exhibits a highly heterogeneous elemental distribution, whereas on fragment C where gilding is exposed, CuKα exhibits a distinct banded elemental distribution (Fig. 8). The Cu K-edge XANES data reveal varying amounts of Cu^+ and Cu^{2+} oxidation states. Notably, a pattern emerges, indicating that copper tends to be consistently in a more oxidized state at the outermost regions of the examined areas (Fig. 8).

3.3. Characterisation of the cross-section on one edge of fragment B by optical/electron microscopy, EDS spectroscopy and EBSD

A BIB cross-section was performed on fragment B (Fig. 1b) to examine the corrosion present and the gilding. The cross-

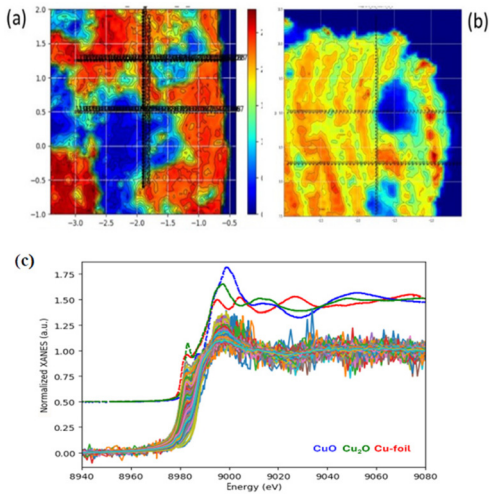

Fig. 8 Two 3 × 3 mm XRF mapping using a 50 micron @12 500 eV beam exhibiting the fluorescence signal distribution of Cu Kα on (a) a heavily corroded C-sample exhibiting a highly heterogeneous elemental distribution and on (b) a gilded C-sample exhibiting a characteristic banded elemental distribution. (c) The Cu K-edge micro-XANES obtained on both samples exhibit a diversity of Cu oxidation states (Cu^{+} and Cu^{2+}). Warmer colours mean higher fluorescence signal from the selected element (source: Josep Roqué Rosell).

section sample cut was achieved so that the two corroded sides can be examined. The surface was then first analysed by means of optical microscopy (Fig. 9).

At least two types of corrosion products, could correspond to two morphologies observed previously (Fig. 4 and 5), with evident needle-like morphologies indicated by the yellow arrows, and at first glance, a more continuous and dense morphology indicated by the red arrows (Fig. 9). Note that a bulk layer of 50–100 μm is visible all along the cross-section, in which flakes with a brassy colouring can be observed (marked with the rectangular area 2). A very thin black layer, identified later as the gold rich layer, with a thickness of less than 1 μm, and barely visible under optical microscopy, is located on top of this bulk layer.

SEM–EDS elemental maps of the cross-section show that the sample is composed of several layers (Fig. 10). The upper corrosion product layer (area 3 in Fig. 9) consists of a copper-rich oxide layer showing a needle like morphology. The needles are around 50 μm long and a few micrometers thick. Those needles arise from a denser layer of the same chemical composition, which thickness is less than 50 μm. Some aggregate, enriched in Si, Ca, Al and K, can be locally found on both surfaces, with sizes of around 5–10 μm. These phases may be linked to soil residues.

The core copper metal contains a small amount of oxygen. A layer of gold a few hundred nanometers thick separates this layer from the more oxygen-enriched surface layer. The EDS spectrum of the Au-rich layer indicates that it also contains a certain amount of Hg (Fig. 6). The gold layer consisted of around 86 wt% Au, 10 wt% Hg and 3 wt% Zr with other traces (see ESI Fig. S1†). At the bottom of the cross-section (corresponding to the inner side of the headgear) a corrosion layer of similar composition is present as evidenced by EDS but includes several micrometric globular particles enriched in sulphur, iron and chlorine.

To further characterize the phases present in this corroded gilded copper, three areas were selected for additional observations:

• The upper corrosion product layer that exhibits a needle shape morphology. As the XRF and SEM observations both indicate that the front and back corrosion layers present the same contrast and chemical composition, it can be assumed that they both are of the same nature, which is indicated as zone 3 in Fig. 9.

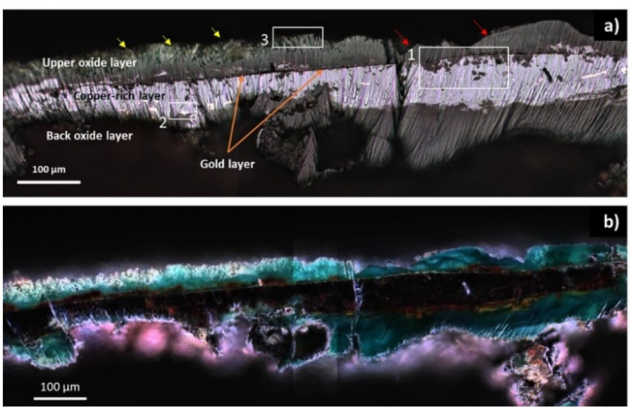

Fig. 9 Optical micrograph of the BIB cross-section. (a) Bright field image and (b) dark field image. Areas 1, 2, and 3 were mapped using EBSD. Yellow arrows indicate evident needle-like morphologies while red arrows highlight an oxidised layer, at first sight more continuous. Under the upper general oxide layer (phases declared Cu, CuO, Cu_2O, azurite and malachite), a very thin black layer was guessed, identified later as the gold rich layer (source: MATEIS/INSA).

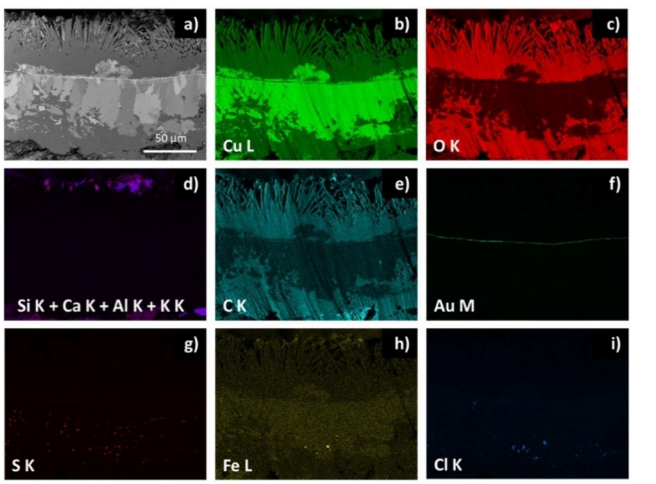

Fig. 10 SEM–EDS maps on the BIB cross-section, (a) SEM–BSE micrograph corresponding to the (b) copper, (c) oxygen (d) silicon plus calcium, plus aluminum and potassium, (e) carbon, (f) gold, (g) sulphur, (h) iron and (i) chlorine elemental maps (source: MATEIS/INSA).

• The gilding layer and the Cu core below as zone 1 and zone 2 in Fig. 9.

• The copper core, to study the nature and distribution of secondary phases located at Cu grain boundaries.

Surface corrosion characterisation by SEM–BSE, EBSD, and 3D-ED. The surface corrosion product consists of needle shaped crystals on its top surface with lengths of a few tens of microns. These needle shaped grains seem to grow on an underlying corrosion layer also a few tens of microns thick. This last layer includes micrometric grains in places close to the gold layer (Fig. 11a). EBSD orientation maps using ASTAR reveal that the needles are very thin, with thicknesses of 500 nm to 1 μm. Neighbouring laths show close orientations, as if they grew up with a given orientation relationship to the previously formed substrate (Fig. 11d). Even if the indexation is not perfect, among all the declared phases declared (Cu, CuO, Cu_2O, azurite and malachite), the needles were indexed as malachite.

Further 3D-ED analysis confirms the malachite structure in the shape of needles (Fig. 12). 3D-ED analysis on several individual phases with a needle morphology revealed unit cell very close to the structure of the malachite mineral $Cu_2(OH)_2(CO_3)$ with monoclinic unit cell a = 9.5 Å, b = 11.97 Å, c = 3.24 Å, and a beta angle of 98.75° (see also ESI S1†). Malachite appears homogeneously dark on SEM–BSE images and appears to grow on top of grains globular in shape, with diameters ranging from 2 to 10 μm and that were indexed as cuprite. The results

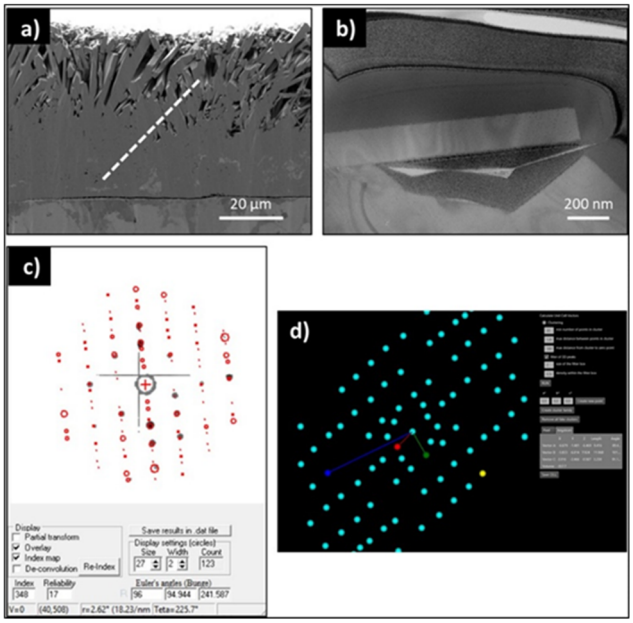

Fig. 12 3D-ED tomography analysis of the needles. (a) SEM imaging with the mark of the FIB lift-out for TEM specimen preparation (white dotted line). (b) STEM bright-field image of a needle crystal where 3D-ED tomography was applied. (c) Good ASTAR matching between monoclinic malachite structure template and experimental ED intensities. (d) Unit cell of monoclinic malachite as determined from ADT (automated diffraction tomography) software (source: MV).

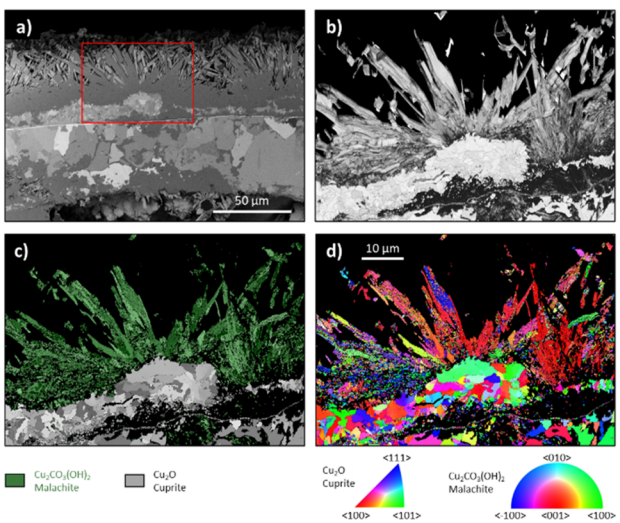

Fig. 11 EBSD orientation maps of the top layer area, with (a) a SEM–BSE micrograph showing the localization of the map. The depth of field available in SEM allows needles to be seen outside the BIB cross-section. These needles appear lighter on the image and they cannot be considered in the EBSD analysis because the geometric conditions are not met. (b) Band contrast map (image quality factor derived from the Hough transformation, which reflects the diffraction quality: the higher the intensity, the better the diffraction pattern). (c) Phase map with malachite in green and cuprite in grey and (d) inverse pole figure in the *Y* direction (IPFY) orientation map, with IPF colour code maps for cuprite (left) and malachite (right) (source: MATEIS/INSA).

reveal that as expected cuprite had formed first, on top of the gold layer, and malachite needles grew on top of the cuprite. Although XRD analysis could provide an additional proof for the presence of cuprite, the samples are not flat, and contain a very large distribution of different phases that would be mixed up in the global XRD analysis. Therefore, our experimental methodology was developed around local characterization methods, such as the ones presented.

Gold-rich layer characterisation using SEM–BSE and 3D-ED TEM–EDS. An overview and a detailed view of the gold layer are shown in Fig. 13a and b, respectively. SEM–BSE imaging shows that the thickness of the gilding layer is at a few hundred nanometers, and that it is made up of nanograins. TEM–EDS measurements performed on a FIB foil extracted through the gilding layer confirms the presence of gold, copper and mercury but also revealed the presence of Fe, Al, and Zr. The chemical composition was found to be heterogeneous through the layer (see ESI S1†).

To analyse the nature of the Au alloy in the thin layer of gilding, 3D-ED tomography was performed in various areas of the thin layer (from −25° to +61°, every 1°) (Fig. 13c for the FIB lamella including the Au layer). Due to the existence of very small crystal domains (*e.g.* up to 50 nm), a number of ED patterns overlapped during tilting. Some of the 2D patterns where no overlapping reflections was present were indexed as cubic Au (a = 4.07 A). A number of ED patterns with overlapping reflections infer a possible local nanostructure of more

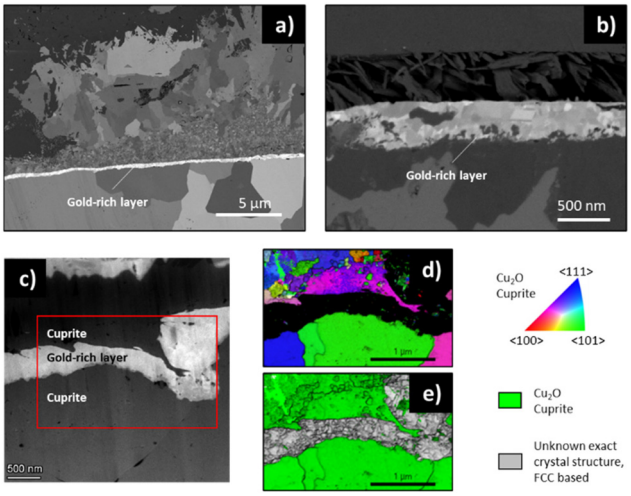

Fig. 13 (a) and (b) Low and high magnification SEM–BSE micrographs of the gold-rich layer. (c) HAADF–TEM micrograph of the layer, and (d) ab ASTAR orientation map, with a resolution of 1–3 nm of the red box region of (c). (e) An ASTAR correlation image, highlighting domains of single orientation. Straight grain boundaries as are expected to be twin boundaries. The gold-rich layer consists of nanograins, whose crystallographic nature could not be identified and with grain size ranging from 50 to 200 nm (source: MATEIS/INSA + MV).

complex, probably ternary Au–Hg–Cu alloy, which we have not been able to identify yet.

ASTAR data were collected from the FIB foil (the red box region in Fig. 13c), which is from the interface between the corrosion and the core metal. Using the ASTAR phase and orientation mapping algorithm, individual ED patterns cannot be indexed on the basis of pure cubic Au, but ED patterns show ordering structures of a gold alloy. The analysis (Fig. 13d and e) was performed using FCC templates, with adapted lattice parameters to match the diffraction patterns from the layer. The "orientation" map shows domains of "single" orientation, which can be used to determine the grain size of the layer ranging from 50 to 200 nm, also supported by the cross-correlation image (Fig. 13e, grey area). No noticeable deformation or orientation in the grain is present, showing that gilding was not deformed during the shaping of the headgear, confirming evidence that gilding was applied after shaping.

Core Cu metal characterization using OM, SEM–BSE, TEM–EDS, EBSD, and ASTAR. EBSD orientation maps were acquired on the central part of the cross-section (rectangle 1 on Fig. 9) to investigate the grain structure and the main nature of the core-metal. On this area, the EBSD acquisition was performed using cuprite as input, and the other corrosion or metallic phases are not indexed on this map. The copper in the core metal consists of grains of different sizes (Fig. 14). Near the gilding layer, large grains with diameters above 30 µm show no particular orientation or texture. The grain size decreases, and a thin layer of much smaller grains is observed towards the other side of the section, which corresponds to the inner side of the headgear (Fig. 14b, red arrows, grain size between 100 and 300 nm). This thin grain layer is not observed all over

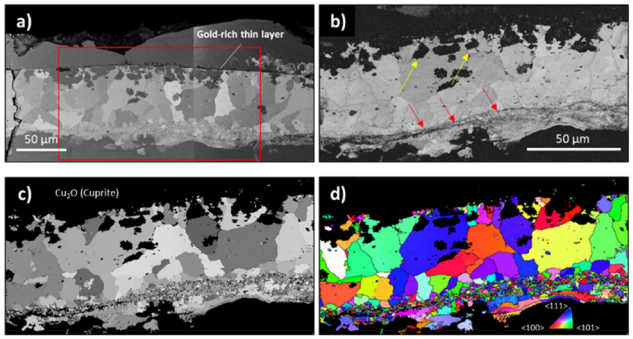

Fig. 14 EBSD orientation maps of the Cu core metal (rectangular area 1 shown in Fig. 4), with (a) SEM–BSE micrograph, (b) band contrast map, (c) phase map with cuprite in grey levels and (d) an IPFY orientation map.

the sample and seems to have disappeared at some places, where it was recovered by the corrosion product layer. Another type of grains is present at the bottom of this layer, elongated grains, where larger disorientation angle can be measured, which is a sign of plastic deformation. Such grain characteristic difference could be the result of a surface deformation during the shaping process of the artifact. The examined fragment carries a four-petal flower leaf decoration likely made by stamping or hammering (Fig. 4), which could explain the deformation observed on this side.

Small areas with crystals inside the cuprite areas were not indexed (Fig. 14b, dark areas indicated by the yellow arrow), as well as some intergranular zones. Those areas are composed of smaller phases that could not be indexed with EBSD mapping. In these polycrystalline areas, some shiny flakes were visible on OM micrographs throughout the cuprite bulk layer (Fig. 9a), and were indexed as copper grains (Fig. 15, and rectangle 2 on Fig. 9). While the identification of the structure cannot strictly be assessed using EBSD, it reveals that each area constitutes a single grain in which slight orientation variations are present. This could be due to the deformation

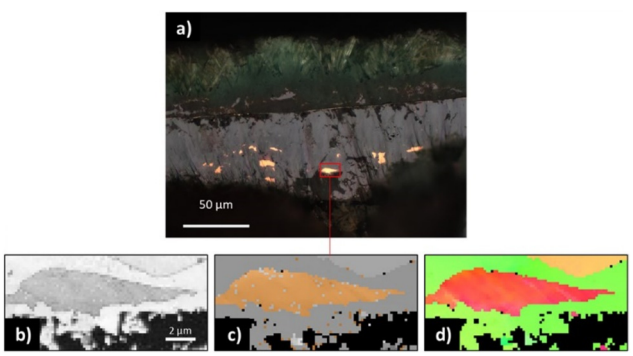

Fig. 15 EBSD analysis of a flake with a brassy colouring within the cuprite bulk layer. (a) OM image showing flakes with a brassy colouring within the cuprite bulk layer flake analysed by EBSD framed in red. (b) Band contrast map, (c) phase map with cuprite in grey and Cu in orange and (d) IPFY orientation map for both phases (source: MATEIS/INSA).

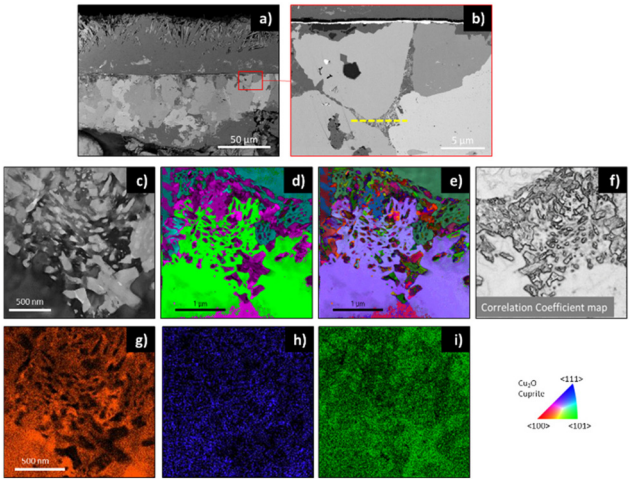

Fig. 16 The presence of an additional phase at the grain boundary for the Cu core metal layer, presenting a eutectic morphology. (a and b) SEM–BSE imaging of the phases observed close to the Au-rich layer. (c) TEM–HAADF micrograph of the area indicated by the yellow line of a. (d) ASTAR phase map: green phase is Au_3Cu, blue $Au_{0.8}Cu_{0.2}$, and purple was indexed (not well) as $AuCu_2$. (e) ASTAR corresponding orientation map. (f) ASTAR–ACOM correlation coefficient map. (g, h and i) TEM–EDS elemental maps for Cu, Au and O, respectively (source: MV).

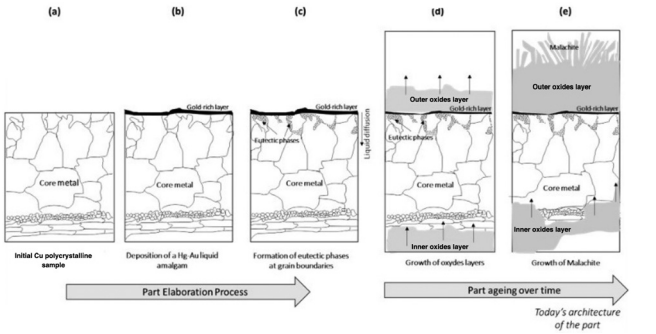

Fig. 17 Proposed mechanism for the formation of the Au-rich layer deposition and ageing over time. Initial elaboration process (a-c) with Cu, Hg-Au deposition and eutectic phases, and later ageing (d, e) including growth of corrosion layers and malachite. The latter represents the current structure of the sample.

process after the solidification or to strain accommodation during the solidification/phase transformation during growth.

Near the gilding layer in the copper core metal and towards the outer side of the headgear, a complex microstructure is observed between grain boundaries, which was not possible to index (like the not-indexed area in Fig. 14). Fig. 16 shows evidence of this nanometric phase between the grain boundaries; the morphology of which is typical of eutectic phases grown because of liquid diffusion. Fig. 16a shows the SEM–BSE image of the cross-section, where the noted red rectangle is visible in Fig. 16b; the gilding layer appears as a yellow line underneath corrosion at the top of the image, whereas the yellow annotated line is investigated further (Fig. 16c–i). Fig. 16g–i shows EDS elemental mapping for Cu, Au and O, respectively, confirming that this is a phase formed during gilding. It is likely that the crystallographic nature of this phase is Au_3Cu, $Au_{0.8}Cu_{0.2}$, and $AuCu_2$ as seen in Fig. 16d.

4. Discussion

The characterization of this piece from a Tang dynasty headgear aims to better understand the manufacturing processes used in the past, as well as to identify the sources of material supply. However, these headgears were buried for hundreds of years after being manufactured and used. It is therefore necessary to analyse the different constituents of this part and identify the corrosion products, which were likely formed during the burial of the headgear, and the metallurgical products resulting from the formation and use of this object.

The analysed part is mainly composed of the following layers, as schematized in Fig. 17e:

(i) On the outer layer (top part), needle-shaped corrosion grains identified as malachite.

(ii) A ~100 nm thick Cu–Au–Hg layer, consisting of nanometer-sized grains.

(iii) Core metal consisting of large (>50–100 µm diameter) Cu-rich grains.

(iv) A layer of nanograins and of elongated deformed grains.

(v) An inner corrosion oxide layer identified as cuprite at the bottom part.

The external layers (i and v) are corrosion product layers that help understand the material's evolution during its burial time, whereas the internal layers (ii–iii–iv) are identified as the initial constituents of the headgear and help understand how it was manufactured and shaped.

4.1. Manufacturing technology and gilding

The main layer consists of copper grains (layer iii), with a size >50 µm in diameter (Fig. 14). These grains, with an FCC structure, mainly contain copper and a small amount of oxygen. They have been identified by SEM–EBSD as cuprite Cu_2O and show no texture or plastic deformation. In some places, residues of ~20 µm in size, with a bright color under optical microscopy, are present and identified as pure copper (Fig. 15). It is therefore plausible to think that the headgear was originally made of almost pure copper, which has oxidized over time, now identified as cuprite Cu_2O (Fig. 17a).

At the bottom of the cross-sectioned sample, nanometer-sized grains showing no plastic deformation, as well as elongated grains parallel to the surface, of the same composition and crystallographic structure as the core material, are present. This elongated morphology is characteristic of a surface treatment such as hammering. Furthermore, when grains are highly deformed and then subjected to elevated temperature, a recrystallization phenomenon may occur, leading to the formation of nanometric grains free of defects.

Thus, these two morphologies (elongated grains and nanometric grains) can be interpreted as signs of plastic surface deformation. This is consistent with the presence of the 4 flower petals observed in Fig. 2, which must have been formed by hammering. It can therefore be concluded that the headgear, originally made of relatively pure copper, was shaped by internal hammering.

Additionally, a thin gold-rich layer was observed on the headgear's external surface (Fig. 17b). Copper, gold and mercury were detected from SEM–EDX and TEM–EDX, but local TEM–ACOM (ASTAR) phase analyses did not evidence the presence of Au nor Hg phases, even when trying to modify the lattice parameters in order to simulate a possible solid solution. It is suggested that a complex intermetallic Cu–Au–Hg compound is present, whose chemical composition and lattice structure were not possible to verify.[46] A detailed structural analysis of this layer, conducted using TEM–ASTAR, reveals the presence of defect-free nanograins without a particular crystallographic structure, indicating that this layer did not undergo plastic deformation. It is therefore unlikely that this layer could have been deposited in a solid state and then plastically deformed on the surface. Furthermore, the presence of eutectic morphology phases (Fig. 16), rich in Au in the subsurface layer, and present at the grain boundaries of cuprite, suggests diffusion of liquid gold–mercury along the copper grain boundaries. This explains the presence of eutectic phases and the grain boundaries in the core metal (Fig. 17c). One can note that almost all over the analysed part, the gold layer is still present at the interface, even if partially recovered by the corrosion product. This demonstrates a very good surface adhesion between the initial copper part and this decoration layer. The solid deposition of layers, as for solid gilding results in lower adherence performance, where the layer would have been partially broken.

During elaboration at the liquid state, it is probable that copper also diffused into the liquid or partially solidified gold layer to form mixed Cu–Au–Hg compounds, which would also contribute to the remarkable adhesion of the layer. Indeed, the Cu–Au equilibrium diagram indicates complete miscibility of Cu in Au at relatively low temperatures, and the formation of mixed Cu–Au–Hg compounds at 300–400 °C.

Finally, the analysis of the object's constituent layers explains the microstructural evolution during its creation (Fig. 17, part elaboration process). The initial material, made of nearly pure copper, was hammered on the internal surface, creating a layer of nanometer-sized grains and elongated grains on the internal surface (Fig. 17a). Then, a liquid Au–Hg amalgam was deposited on the external surface (Fig. 17b), and some of the gold diffused along the grain boundaries in a liquid state to form eutectic phases. Simultaneously, probable copper diffusion into this gold layer led to the formation of a yet unidentified Cu–Au–Hg type of compound on the surface.

4.2. Corrosion phenomena and aging during burial

The analysis of declared copper oxide/carbonate structures and morphologies on the surface helps understand the piece's structural evolution during its burial, explaining its current microstructure. It is therefore plausible to think that the part that was the most affected by the corrosion phenomena is the external part (the one made of gold), which was very quickly in contact with the soil and dirt. The gold-rich layer is, quite surprisingly, still present along the object. It has been largely covered by a corrosion product and is no longer visible on the surface but is still present almost uniformly, indicating very good adherence to the headgear.

It is covered by a relatively thick corrosion product layer, which is green in appearance under optical microscopy (Fig. 9). XANES–XRF analysis shows the presence of different oxidation states and thus different types of oxides on the entire surface. Using EBSD, part of this oxide has been identified as cuprite, which is composed of grains >10 μm in size, untextured and underformed (Fig. 11), on which lamellar corrosion products with a particular orientation and identified as malachite have grown. A first oxide layer (cuprite) likely nucleated on the gold-rich layer, aided by the diffusion of copper from the headgear and through the gold-rich layer. Indeed, the layer is relatively thin (~100 nm), which was then probably composed of Cu–Au–Hg compounds with an equilibrium composition and with nanosized grains. It therefore contains a huge amount of grain boundaries that help Cu diffusion towards the surface. Later, a second structure, malachite, nucleated on this layer with a needle-like morphology.

On the internal side of the piece, a corrosion product layer formed by dissolving the headgear, explaining the disappearance of nanometric grains and elongated grains in some areas. Copper dissolution and migration outwards take place during corrosion, and it forms corrosion products on the surface of the metal in archaeological timescales.[43]

The external layer is generally of fairly constant thickness (~80 μm), whereas the thickness of the internal corrosion product layer and the residual copper layer varies greatly (Fig. 9), indicating different local oxide growth rates.

Thus, the piece's evolution after burial can be schematically described by the steps presented in Fig. 17, part aging over time. First, an external corrosion product layer grew on the gold and mercury-rich layer, and internal growth at the expense of the constitutive material (Fig. 17d), followed by the appearance of needle-like morphology on the extreme surface (Fig. 17e).

4.3. Outcomes, historical

This studied artifact alloy is unique in ancient metallurgical technology in China; from the first microscopy examination it was proved that it was a gilded thin layer of deformed Cu-based metal. However, the study of ancient gilding is often problematic, as the gilding layers are soft and prone to deformation during sample preparation. In this respect, broad ion beam (BIB) and focused ion beam (FIB) milling on a field emission gun scanning electron microscope (FEG–SEM) provides quasi-non-invasive *in situ* sampling. The crystallographic phases obtained by EBSD acquisitions revealed several possible mineral phases in the corrosion products.[49] Relevant

archeometallurgical investigations have been reported during the past 3000 years elsewhere.[50–52]

The headgear was made of pure copper metal, the hammering of which left evidence of relatively large grains in the core metal (several hundred micrometers). The presence of a thin layer of nanometric grains on the lower outer part, as well as elongated, aligned grains showing plastic deformation, provides evidence that the object was shaped from the lower part of the piece. The sign of plastic deformation is evidence of hammering, supported also by the repousse four leaf decoration.

Amalgam gilding was applied to the outer part (shown at the top of the diagram) (Fig. 17b), to decorate the headgear. It is important that with this methodology and advanced characterization techniques we were able to visualize the evidence of gilding at the nanometre scale.

The gold layer consists of an Hg–Au alloy, where mercury can be associated with the metallurgy of gold in the Tang dynasty China. The Huachanggou gold deposit, which is located in the Lueyang County, Shaanxi Province in central China, contains gold deposits[47] with rich ore deposits in minerals associated with gold and copper. Xi'an (Shaanxi province) is neighbour to Sichuan Province (with the famous Lengfangou copper mine). In Xian Shaanxi several important ores exist for gold that are associated with secondary galena and zircon.[48] In Qinling mountains (south of Xian, Shaanxi, the geographical dividing line between Northern China and Southern China) important deposits of gold and galena are found in particular in the Xiaoqinling–Xiong'ershan region in eastern Shaanxi and western Henan provinces, central China.

5. Conclusion

This work reveals that the metal headgear from the tomb of a female in the Tang dynasty period is made of copper, and its shaping method and hammered decoration resulted in nano-sized grains at the outer part of the side that would be the inner part of the headgear. The analysis of three fragments (A, B, and C) using specific techniques revealed highly heterogeneous elemental distribution.

It was gilded using the mercury-amalgamation method, and liquid diffusion resulted in the formation of intermetallic compounds. A eutectic phase is also observed in the grain boundaries. To the best of our knowledge, it is the first time that these nano-scale phases are noted on archaeological timeframe objects. The crystallographic investigation provided useful input on the growth of malachite needle-like crystals on a layer of cuprite on the surface of the corroded fragment.

Analysis of more archaeological samples would confirm how common these structures are during corrosion in the ground. Future work will include further analysis to identify the specific nature of the copper, gold, and mercury intermetallic compounds combined with ICP-MS for elemental composition analysis of the materials of interest. Overall results of this scientific analysis point out that the craftsmen employed sophisticated techniques in the making of funerary goods in the Tang dynasty.

Author contributions

Conceptualization, I. L.; methodology, S. C., T. D., M. V., J. R.-R., C. M., P. P. D., and S. N.; software, S. C., M. V., J. R.-R., C. M., A. G.-P., and A. S. G.; validation, S. C., T. D., M. V., J. R.-R., P. P. D., A. S. G., P. M., J. Y., and X. Z.; formal analysis, S. C., T. D., M. V., J. R.-R., C. M., P. P. D., A. G.-P., and A. S. G.; investigation, I. L., S. C., T. D., M. V., J. R.-R., C. M., P. P. D., A. G.-P., A. S. G., S. N., and P. M.; resources, I. L., S. C., M. V., J. R.-R., S. N., and X. Z.; data curation, S. C., M. V., P. P. D., and A. S. G.; writing—original draft preparation, I. L. and S. N.; writing—review and editing, I. L., S. N., P. M., S. C., M. V., J. R.-R., J. Y., and X. Z.; visualization, S. C., J. R.-R., M. V., P. P. D., and S. N.; supervision, I. L., M. V., S. N., J. Y., and X. Z.; project administration, I. L. and S. N. All authors have read and agreed to the published version of the manuscript.

Data availability

Data are available upon request from the authors.

Conflicts of interest

There are no conflicts to declare.

Acknowledgements

The authors acknowledge the 'Réseau Renatech' and the assistance of David Troadec in the preparation of the FIB thin foils at IEMN (**https://www.renatech.org/**). IL is thankful for support for the Sino-Hellenic Academic Project (**https://www.huaxiahellas.com**) from the Key Research Institute of Yellow River Civilization and Sustainable Development & Collaborative Innovation Center on Yellow River Civilization of Henan Province, Henan University, China.

References

1 W. A. Oddy, *Endeavour*, 1991, **15**, 29.
2 W. A. Oddy, in *Met. Plat. Patination*, ed. S. L. Niece and P. Craddock, Butterworth-Heinemann, 1993, pp. 171–181.
3 S. Lim and S. Kang, *J. Korean Conserv. Sci. Cult. Prop.*, 1992, **1**, 60.
4 P. Jett, in *Met. Plat. Patination*, ed. S. L. Niece and P. Craddock, Butterworth-Heinemann, 1993, pp. 193–200.
5 K. Anheuser, *Archaeometry*, 2000, **42**, 189.
6 Y. Shao, F. Jiang and J. Yang, *Archaeol. Anthropol. Sci.*, 2024, **16**, 51.

7 L. Deng, X. Ouyang, J. Jin, C. Ma, Y. Jiang, J. Zheng, J. Li, Y. Li, W. Tan and R. Yang, *Anal. Chem.*, 2013, **85**, 8594.
8 C. Lee, *J. Hist. Fu Jen Cathol. Univ.*, 2013, **30**, 1.
9 G. Masi, C. Chiavari, J. Avila, J. Esvan, S. Raffo, M. C. Bignozzi, M. C. Asensio, L. Robbiola and C. Martini, *Appl. Surf. Sci.*, 2016, **366**, 317.
10 R. Cesareo, *X-Ray Spectrom.*, 2019, **48**, 202.
11 Y. Shao, F. Jiang, J. Yang, Q. Zhang, X. Lu, W. Fu and S. Yu, *Heritage Sci.*, 2023, **11**, 162.
12 T. Drayman-Weisser, A. I. for C. of Historic and A. Works, *Gilded Metals: History, Technology and Conservation*, Archetype Publications, 2000.
13 N. Laskaris, I. Varalis, C. Tsodoulos and C. Dolmas, *Medit. Archeol. Archaeom.*, 2020, **20**(1), 189–189.
14 J. Sáenz-Samper and M. Martinón-Torres, *Antiquity*, 2017, **91**, 1253.
15 V. Singh and S. Singh, in *Proc. INTERIM Meet. ICOM-CC Met. Work. GROUP Sept. 26–30 2016 NEW DELHI INDIA*, ed. M. Raghu, C. Claudia and P. Achal, 2016, pp. 46–53.
16 V. Leusch, B. Armbruster, E. Pernicka and V. Slavčev, *Cambridge Archaeol. J.*, 2015, **25**, 353.
17 Y. Liu, J. Yang and P. Tan, *Sci. Conserv. Archaeol.*, 2019, **31**, 75.
18 Z. Yao, *Huaxia Archaeol.*, 2019, **5**, 113.
19 D. Gao, F. Li, J. Song, X. Xu, Q. Zhang and L. Niu, *Talanta*, 2009, **80**, 479.
20 P. A. Lins and W. A. Oddy, *J. Archaeol. Sci.*, 1975, **2**, 365.
21 J. J. Zhao, R. Liu and Y. Lü, *Daxue Huaxue*, 2021, **36**, 39.
22 G. M. Ingo, G. Guida, E. Angelini, G. Di Carlo, A. Mezzi and G. Padeletti, *Acc. Chem. Res.*, 2013, **46**, 2365.
23 G. M. Ingo, C. Riccucci, M. Pascucci, E. Messina, C. Giuliani, P. Biocca, L. Tortora, G. Fierro and G. Di Carlo, *Appl. Surf. Sci.*, 2018, **446**, 168.
24 R. Margreiter, J. Baumann, I. Mantouvalou, M. Radtke, U. Reinholz and E. Strub, *Archaeometry*, 2022, **64**, 1465.
25 T. Kobiela, B. Nowakowski and R. Duś, *Appl. Surf. Sci.*, 2003, **206**, 78.
26 Z. Yao and Y. Gong, *Heritage Sci.*, 2019, **7**, 72.
27 G. Demortier, *Sci. Cult.*, 2021, **7**, 13.
28 Y. Salem and E. A. Allah, *Scientific Culture*, 2021, **7**, 65.
29 F. Di Turo, *J. Cult. Heritage*, 2020, **43**, 271.
30 E. Figueiredo, R. J. C. Silva, M. F. Araújo and J. C. Senna-Martinez, *Microchim. Acta*, 2010, **168**, 283.
31 *Metallurgy and Civilisation*, ed. J. Mei and T. Rehren, Eurasia and Beyond, 2009.
32 I. Liritzis, N. Laskaris, A. Vafiadou, I. Karapanagiotis, P. Volonakis, C. Papageorgopoulou and M. Bratitsi, *Sci. Cult.*, 2020, **6**, 1.
33 I. Liritzis, *Proc. Eur. Acad. Sci. Arts*, 2024, **3**, 1–12.
34 S. Pang and C. S. Xu, in *Methods Cell Biol*, ed. K. Narayan, L. Collinson and P. Verkade, Academic Press, 2023, pp. 269–300.
35 G. D. West and R. C. Thomson, *J. Microsc.*, 2009, **233**, 442.
36 J. Portillo, E. F. Rauch, S. Nicolopoulos, M. Gemmi and D. Bultreys, *Mater. Sci. Forum*, 2010, **644**, 1.
37 S. Nicolopoulos, P. P. Das, P. J. Bereciartua, F. Karavasili, N. Zacharias, A. Gómez Pérez, A. S. Galanis, E. F. Rauch, R. Arenal, J. Portillo, J. Roqué-Rosell, M. Kollia and I. Margiolaki, *Heritage Sci.*, 2018, **6**, 64.
38 S. Nicolopoulos, P. P. Das, A. G. Pérez, N. Zacharias, S. T. Cuapa, J. A. A. Alatorre, E. Mugnaioli, M. Gemmi and E. F. Rauch, *Scanning*, 2019, **2019**, e4870695.
39 M. Gemmi, E. Mugnaioli, T. E. Gorelik, U. Kolb, L. Palatinus, P. Boullay, S. Hovmöller and J. P. Abrahams, *ACS Cent. Sci.*, 2019, **5**, 1315.
40 E. Mugnaioli, T. Gorelik and U. Kolb, *Ultramicroscopy*, 2009, **109**, 758.
41 L. Simonelli, C. Marini, W. Olszewski, M. Ávila Pérez, N. Ramanan, G. Guilera, V. Cuartero and K. Klementiev, *Cogent Phys.*, 2016, **3**, 1231987.
42 U. Bergmann, L. Bertrand, N. P. Edwards, P. L. Manning and R. A. Wogelius, in *Synchrotron Light Sources Free-Electron Lasers*, ed. E. Jaeschke, S. Khan, J. R. Schneider and J. B. Hastings, Springer International Publishing, Cham, 2019, pp. 1–63.
43 L. Robbiola, J.-M. Blengino and C. Fiaud, *Corros. Sci.*, 1998, **40**, 2083.
44 P. Manti and D. Watkinson, *J. Cult. Heritage*, 2022, **55**, 158.
45 M. Nicholas and P. Manti, in *ICOM-CC 17th Trienn. Conf. Prepr. Melb. 15–19 Sept. 2014*, ed. J. Bridgland, ICOM, Paris, 2014, p. 13.
46 K. Chudnenko and G. Pal'yanova, *Thermochim. Acta*, 2013, **566**, 175.
47 C. Liu, J. Liu, E. J. M. Carranza, L. Yang, J. Wang, D. Zhai, Y. Wang, J. Wu and H. Dai, *Ore Geol. Rev.*, 2016, **73**, 354.
48 Y.-M. Zheng, T. Liu, J. Jiang, L. Yang, Y. Fan, A. T. S. Wee and J. P. Chen, *J. Colloid Interface Sci.*, 2011, **356**, 741.
49 A. Vaitkus, A. Merkys, T. Sander, M. Quirós, P. A. Thiessen, E. E. Bolton and S. Gražulis, *J. Cheminf.*, 2023, **15**, 123.
50 O. Çakaj, N. Civici, G. Schmidt and E. Qoku, *Sci. Cult.*, 2023, **9**, 2.
51 M. Rifai, A. Elshahawi and Z. A. Hamid, *Sci. Cult.*, 2023, **9**, 1.
52 Y. Salem and E. Abd Allah, *Sci. Cult.*, 2021, **7**, 3.